pH Stimuli-Responsive, Rapidly Self-healable Coatings Enhanced the Corrosion Resistance and Osteogenic Differentiation of Mg-1Ca Osteoimplant

Dandan Xia, Zhaojun Jia, Yunong Shen, Yufeng Zheng,* Yan Cheng, Pan Xiong,* Shaokang Guan, Yuqian Xu, Fan Yang, Yunsong Liu,* and Yongsheng Zhou*

Mg-Ca alloys have emerged as a promising research direction for biomedical implants in the orthopedic field. However, their clinical use is deterred by their fast corrosion rate. In this work, a pH stimuli-responsive silk-halloysite (HNT)/phytic acid (PA) self-healing coating (Silk-HNT/PA) is constructed to slow down the corrosion rate of Mg-1Ca alloy and its cell viability and osteogenic differentiation ability are enhanced. The Silk-HNT/PA coating exhibits appealing active corrosion protection, by eliciting pH-triggerable self-healing effects, while simultaneously affording superior biocompatibility and osteogenic differentiation ability. Moreover, in vivo studies by histological analysis also demonstrate better osseointegration for the Silk-HNT/PA coated Mg-1Ca alloy. In summary, the Silk-HNT/PA coating in the present study has great potential in enhancing the biomedical utility of Mg alloys.

1. Introduction

Magnesium (Mg) alloys have attracted a great deal of attention for orthopedic implants, due to their appreciable biodegradability, preferable mechanical properties, and intrinsic biocompatibility.[1] However, their rapid degradation in physiological environments can lead to unfavorable issues, which seriously hamper the application of Mg alloys. These include the accumulation of a large amount of hydrogen in the tissue, the loss of mechanical integrity in an early stage, and the production of local alkalinity.[2]

Surface treatment is an effective tactic to enhance the corrosion resistance of Mg alloys. It aims to form a protective layer on Mg alloy surfaces that can avert the direct contact between Mg alloys and the physiological environment.[3] The choice of a suitable surface treatment method is essential to achieve the desired corrosion resistance of magnesium alloys and endow them with wanted functionalities.[4,5] Recently, micro-arc oxidation (MAO), [6] alkaline heat treatment,[7] ion implantation,[8] fluoride treatment,[9] polymer coatings, [10] ceramic coatings,[11] and other methods[12] have been developed on Mg alloys. The resulting coatings generally improve the corrosion resistance of Mg alloys by providing sacrificial physical barriers, and they often suffer from severe local corrosion and even premature coating failures, due to defects such as pits and cracks.

Self-healing coatings, a type of smart coatings that can respond to stimulation of itself or an external environment

D. Xia
Department of Dental Materials
Peking University School and Hospital of Stomatology
Beijing 100081, China

D. Xia, Y. Xu, F. Yang, Y. Liu, Y. Zhou
National Center of Stomatology
National Clinical Research Center for Oral Diseases
National Engineering Research Center of Oral Biomaterials and Digital Medical Devices
Beijing Key Laboratory of Digital Stomatology
Research Center of Engineering and Technology for Computerized Dentistry Ministry of Health
NMPA Key Laboratory for Dental Materials
Beijing 100081, China

Z. Jia
School of Biomedical Engineering
Sun Yat-sen University
Guangzhou 510006, China

The ORCID identification number(s) for the author(s) of this article can be found under https://doi.org/10.1002/smll.202106056.

DOI: 10.1002/smll.202106056

Y. Shen, Y. Zheng
School of Materials Science and Engineering
Peking University
Beijing 100871, China
E-mail: yfzheng@pku.edu.cn

Y. Cheng, P. Xiong
Biomed-X Center
Academy for Advanced Interdisciplinary Studies
Peking University
Beijing 100871, China
E-mail: xiongpan@pku.edu.cn

P. Xiong
The Science and Technology Bureau of Chengdu
(Chengdu Administration of Foreign Experts Affairs)
Chengdu 610042, China

S. Guan
School of Materials Science and Engineering
Zhengzhou University
Zhengzhou 450001, China

Y. Xu, F. Yang, Y. Liu, Y. Zhou
Department of Prosthodontics
Peking University School and Hospital of Stomatology
Beijing 100081, China
E-mail: liuyunsong@hsc.pku.edu.cn; kqzhouysh@hsc.pku.edu.cn

and recover the coating properties have received growing attention.[13,14] An anti-corrosion self-healing coating typically consists of a matrix coating, and corrosion inhibitors (self-healing agents) and their carrier. Most self-healing coatings for industrial applications comprise corrosion inhibitors such as cerium (Ce) ions,[15] 8-hydroxyquinoline,[16] benzotriazole[17], and so on. These are toxic or lack for bioactivity, and thus are not suitable for biomedical applications. It is therefore a desire need to develop bio-related functional self-coatings, which possess biocompatible corrosion inhibitors and bioactive matrix or reservoir coatings, thus simultaneously imparting active substrate protection, necessary biocompatibility, and application-related biofunctionality (e.g., osteo-conductivity/inductivity for orthopedic implants).

Pleasingly, significant efforts have been devoted to addressing the above-mentioned issues. Dong et al. fabricated a dicalcium phosphate dihydrate (DCPD) self-healing coating on pure Mg. These coatings exhibited both self-healing behaviors and good biocompatibility.[18] However, the self-healing efficiency in the long run require further investigation, while the lack of a biofunctional coating component might restrict their applications in orthopedics. Li et al. attempted to develop a multifunctional self-healable coating that can enhance both the corrosion resistance and osseointegration of Mg-based implants. They employed fluoride (F^-) ions as corrosion inhibitors, which, together with curcumin (a natural osteoimmunomodulatory agent), were encapsulated in mesoporous silica nanocontainers and applied onto Mg alloy substrate using a poly-L-lactide reservoir coating. The F ions released locally could react with Mg^{2+} to give a corrosion-resistant MgF_2 layer, while the liberation of curcumin afforded appreciable osteopromotive functionality.[19]

In our previous work, we produced silk fibroin-based self-healing coatings that were added with K_3PO_4 or phytic acid (PA).[20,21] In the designs, K_3PO_4 or PA function as effective and biosafe self-healing agents, while silk fibroin act as their loading vehicle. In addition, silk fibroin harbors intrinsic osteogenic capability owing to its collagen-memetic fibrillar structure. Nonetheless, the direct encapsulation of inhibitors into silk matrix is associated with relatively low loading efficiency, and as a result, undesirably slow kinetics (>18 hours) for completing self-healing.[21] In the present study, we aimed to circumvent this limitation by introduction of halloysite nanotubes ($Al_2Si_2O_5(OH)_4 \cdot 2H_2O$, HNT) as vehicles for self-healing agents. Nanotubular HNT is an emerging nanomaterial carrier for imparting sustained drug delivery. Its inner alumina and outer silica surface layers as well as hollow channels,[22] have been leveraged to abundantly load and sustainably release corrosion inhibitors for aluminum alloys in industry.[23] However, the use of HNT to locally deliver healing agents for biomedical applications has been rarely studied. Herein, the HNT noncarriers were charged with biocompatible corrosion inhibitors PA, and then dispersed into a silk coating, which was applied onto fluoridated Mg-1Ca alloy by spinning assembly. Notably, the fluoride conversion film served as a primary barrier, while the inhibitor loaded HNT afforded active long-lasting anti-corrosive performances. And an additional silk outer coating was employed to provide a secondary barrier and increase osteogenic activity. These led to a sandwich-like, pH stimuli-responsive self-healing coating system, as illustrated in **Scheme 1**. A similar coating that contained Ce ions as inhibitors was prepared, serving as a reference for the self-healing potency of the PA-based system. The degradation rate and self-healing behaviors of the resultant coatings were confirmed in vitro. In addition, the osteogenic differentiation properties of the coated alloy materials were systematically evaluated, both in vitro and in vivo.

2. Results and Discussion

2.1. The Improved Loading Efficiency of HNT

As shown in **Figure 1**A, the HNT had an outer diameter of about 50 nm, an inner diameter of about 15 nm, and a length of 1~3 μm. The size is consistent with the previous study.[24] Figure 1B shows TEM images of HNT loaded with corrosion inhibitors. Compared with the unloaded HNT, significant structural distortions, alongside the loss of transparency, were observed for HNT/X (PA, Ce^{3+}). The cross-section of samples illustrated that HNT/PA almost fully filled the inner lumen of HNT (red circle mark in Figure 1B). For HNT/Ce^{3+} group, the lumen wall of HNT became rough with small burrs. To further ascertain the successful loading of corrosion inhibitors into HNT, coating-relevant elements were characterized by TEM-EDX and XPS. For the former, a point (triangle, Figure 1B) on HNT was selected, with results summarized in Table S1, Supporting Information. For the latter, the XPS survey and high-resolution spectra of HNT/X were acquired and are shown in Figure 2D. In both cases, the relevant characteristic elements of the loaded substance, namely P elements in HNT/PA, and Ce elements in HNT/Ce^{3+}, were detected. The solution before and after loading was collected and the concentrations of characteristic elements were measured to calculate the loading efficiency of inhibitors into HNT. As shown in Figure 1C, the loading efficiency of HNT for PA reached 15.2% ± 1.0%, while the value for Ce^{3+} is 6.3% ± 2.0%. The loading efficiency of HNT for PA is much higher than that for Ce^{3+}. This indicated that the loading efficiency inside the lumen was higher than outside the pipe wall. HNT has a positively charged inner lumen surface and a negatively-charged pipe wall, which respectively show electrostatic affinity towards PA and Ce^{3+}.[22] According to the electrostatic attraction principle, PA with negative charges is easier to enter the interior of the HNT lumen and be loaded through the lumen. However, Ce^{3+} is positively charged, which is to be easily combined with the outer wall of HNT with negative charge. Therefore, the different loading efficiency between PA and Ce^{3+} was detected.

2.2. Coating Characterization

The Silk-HNT/X coatings' surface morphology was observed by SEM images in **Figure 2**A, with no visible cracks on the surface. The thickness of the coatings is about 950±10 nm by measuring the cross-section, as shown in Figure 2B. XPS analysis illustrated the chemical compositions of the coating surface. As shown in Figures 2C and 2D, the major elements of the coating were C, N, and O, which are originated from silk fibroin. ATR-FTIR was used to analyze the functional groups of pure silk and silk-HNT/X. As shown in Figure 2B, the amide characteristic peaks of silk fibroin were observed. In addition,

ADVANCED
SCIENCE NEWS
www.advancedsciencenews.com

NANO · MICRO
small
www.small-journal.com
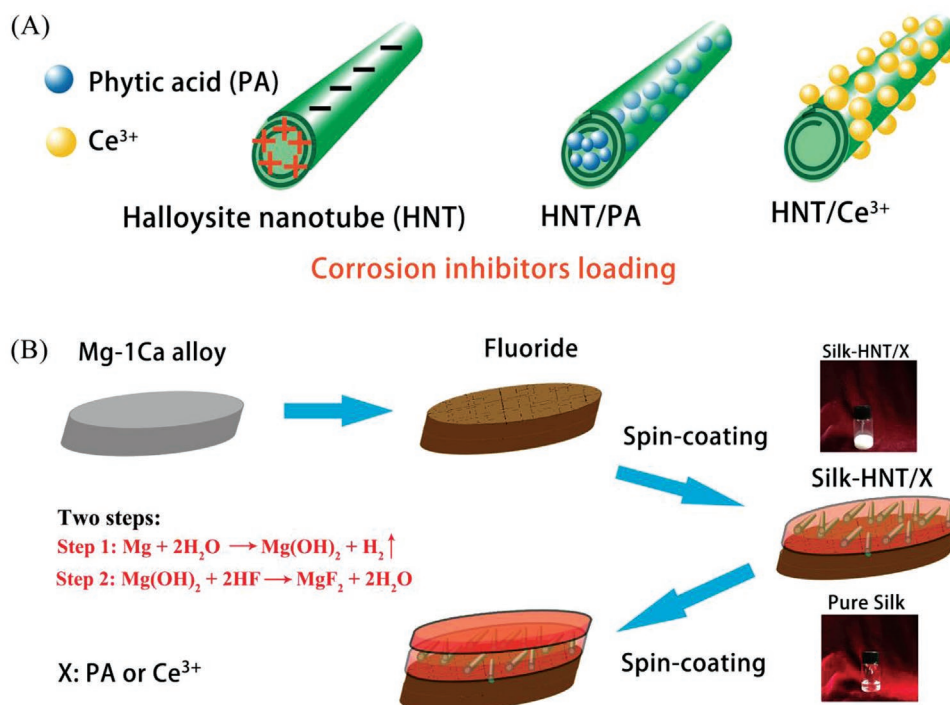
Scheme 1. Schematic illustration of the fabrication process for Mg-1Ca alloy with a sandwiched composite coating.

the SiO_2-OH peak at 1150 cm^{-1} and the Si-OH peak at 3300 cm^{-1} confirmed the existence of HNT within coatings. The secondary structure of silk is crucial to the stability of the resulting coatings. Therefore, we deconvoluted the C peaks of different coatings for silk fibroin secondary structure, with results summarized in Table S2, Supporting Information. It can be seen that, irrespective of HNT addition, all silk-based coatings had high β-sheet structure (~34%) and low random curl ratio, indicative of good coating stability in aqueous solutions. This can be attributed to the unique solvent of silk fibroin in this work and the nature of spin coating method. Studies have found that the use of hexafluoroisopropanol (HFIP) as the solvent promoted the formation of β-sheet structure of silk fibroin,[25] and so did it for the spin coating method.[26] Figure 2E shows the C 1s high-resolution spectra of each group. The C–C, C–H, and C=O bonds of each group shared similar proportions, indicating that HNT had negligible effect on silk structure. Taken together, the prepared coatings were uniform and stable, providing basis for imparting favorable corrosion resistance to Mg-1Ca alloys. From another perspective, the mentioned silk structure endowed the coating with good mechanical properties.

2.3. The Enhanced Corrosion Resistance of Silk-HNT/PA Coating

The in vitro corrosion behavior of the sample was evaluated by immersing the samples in Hank's solution for 30 days. As shown in **Figure 3**A, the amount of hydrogen evolution by the Silk and Silk-HNT/X groups were relatively small compared with the untreated Mg-1Ca alloy and fluorinated samples. The same trend could be seen in the pH value of the solution, as

shown in Figure 3B. These results indicated that the silk-based coatings can effectively improve the corrosion resistance of Mg-1Ca alloy implants. For the macrography characteristic of immersed samples (Figure 3C), there were large amount of corrosion products on the untreated Mg-1Ca alloy surface, while the degrees of corrosion slowed down for the Fluoride and the Silk group. Surprisingly, the Silk-HNT/X groups hold nearly intact surface. SEM images of sample surface can be seen in Figure 3D, the untreated Mg-1Ca alloy underwent local corrosion, with large amounts of corrosion product aggregates on the sample surface. Though fluoride treatment and silk fibroin coating improved the corrosion resistance of Mg-1Ca alloy, local corrosion occurred, as indicated by serious corrosion pits and massive corrosion product formation on the sample surface. Only a few tiny shallow pits appeared on the surface of Silk-HNT/Ce^{3+}, but they did not deepen and propagate. The SEM observation of samples' cross-section (Figure 3E) showed the same corrosion trend that the Silk-HNT/PA and Silk-HNT/Ce^{3+} groups maintained almost integrity.

The EDS results (Table S3, Supporting Information) showed that the corrosion products were carbonates, phosphates, or hydrogen phosphates. A higher proportion of P and Ca was detected on the surface of Silk-HNT/PA, indicating that the coating is more conducive to the deposition of CaP compounds. In addition, the Ca/P ratio is 1.41, which is close to that of hydroxyapatite in natural bone (1.67).[27] ATR-FTIR results (**Figure 4**A) show that the surface of the unmodified Mg-1Ca alloy was mainly comprised of carbonate and hydrogen phosphate, while that of other groups was mainly phosphate. XPS survey spectrum in Figure 4B shows that the major elements on each sample surface were Mg, O, Ca, C, and P. Through the analysis of C 1s high-resolution spectra, it is found
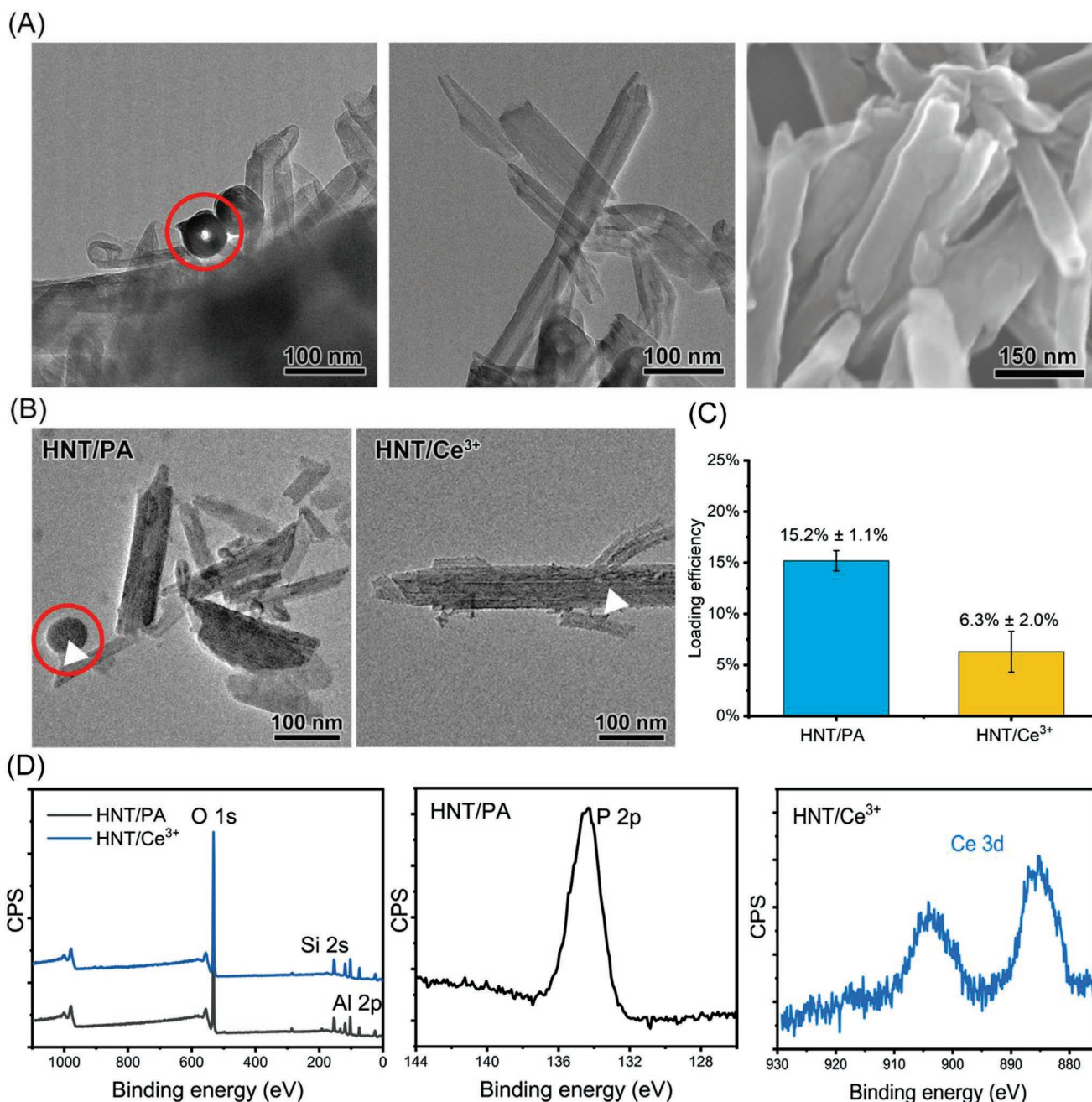
Figure 1. Characterizations of physical and chemical properties of HNT. A) TEM and SEM images of HNT, B) TEM images of HNT/X, C) Loading efficiency of the Silk-HNT/PA and Silk-HNT/Ce^{3+}, D) Binding energy of the Silk-HNT/PA and Silk-HNT/Ce^{3+}.

that the element C of Silk-HNT/X group is mainly derived from silk fibroin, because the proportion of C–C, C–H and C=O bonds is comparable to that before immersion (Figure 4C–G). In addition, a small portion of CO_3^{2-} was also detected.

After immersion for 30 days, the untreated Mg-1Ca alloy, fluorinated samples, and Silk samples underwent severe local corrosion, while the Silk-HNT/PA and Silk-HNT/Ce^{3+} samples maintained their integrity. The reason for the difference is that the Silk-HNT/PA and Silk-HNT/Ce^{3+} sample achieved self-healing, in only 15 min. In our previous study, Silk-PA coating completed self-healing in 18 h, which was much longer

than that of the Silk-HNT/PA and Silk-HNT/Ce^{3+} group in this study.[20] The rapid self-healing is mainly attributed to the improvement in loading efficiency by HNT, which then effectively reduced the healing time. PA is an organic molecule extracted from plants, and it is biosafe and biocompatible. PA has a strong complexation with Mg^{2+} and thus has prompted study and intrigue in surface modification of Mg alloys.[28–30] Ce^{3+} is a frequently used corrosion inhibitor in the industrial field,[31,32] however, its biosafety remains unclear. Thus, we chose the PA as the corrosion inhibitor of interest, while Ce^{3+} as the control to help justify the self-healing ability of PA.
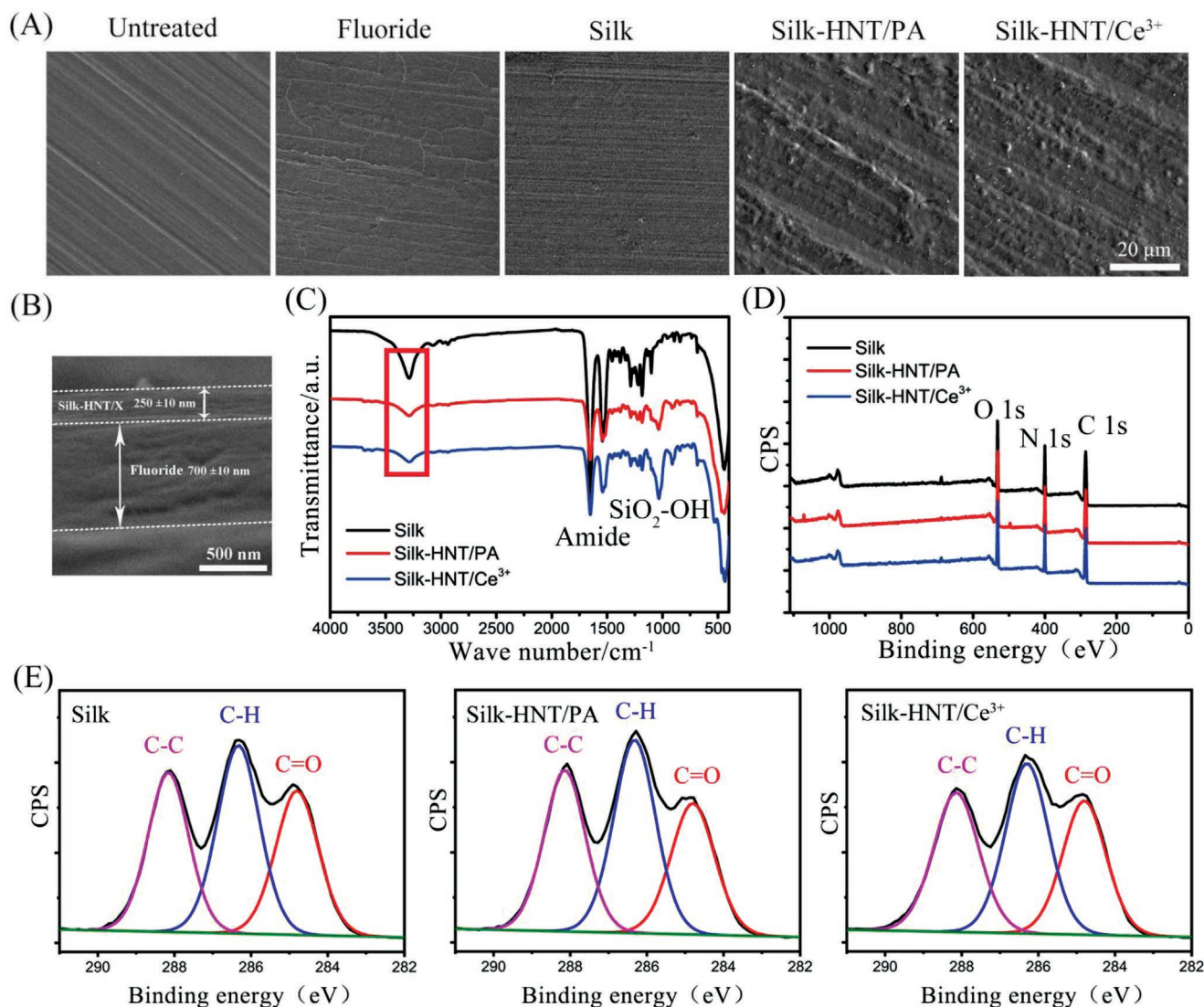
Figure 2. Surface characteristics of prepared coatings. A) SEM images of the untreated, fluoride, silk, Silk-HNT/PA and Silk-HNT/Ce³⁺ surface, B) SEM images of the Cross-section of Silk-HNT/X coating, C) ATR-FTIR spectra of the Silk-HNT/PA and Silk-HNT/Ce³⁺, D) XPS analysis of the Silk-HNT/PA and Silk-HNT/Ce³⁺, E) the co-responding core-level spectra for C 1s of the Silk-HNT/PA and Silk-HNT/Ce³⁺.

When a defect occurred on Mg-1Ca alloy surface, local pH value increased and Mg^{2+} aggregated in the surrounding environment. Then, the Silk-HNT/PA coating responded promptly to the alkaline surface and released phytate ions ($C_6H_xO_{24}P_6^{-(18-x)}$). The latter reacted with Mg^{2+} and formed stable phytin, which would deposited on the Mg-1Ca alloy surface to prevent corrosion propagation.[20] Based on the above analyses, the plausible process of self-healing was proposed (Figure S1, Supporting Information). The chemical reactions involved is summarized as the following equations:

$$yMg^{2+} + C_6H_xO_{24}P_6^{-(18-x)} \rightarrow (Mg)_y C_6H_xO_{24}P_6 \downarrow \qquad (1)$$
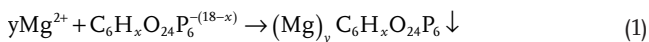
The pH stimuli-responsive behavior of Silk-HNT/PA coating is primarily due to the reconfigurable secondary structure of silk fibroin-based coatings. As shown in Table S2, Supporting Information, the β-sheet structure of silk fibroin was 35%,

while the residual random coils and α-helical structure endowed the coatings with reversible structural transformation ability. As corrosion occurs, the environmental pH rises, and consequently, the residual random coils and α-helical structure in silk fibroin will be stretched due to increased negative charges. As a result, the HNT loaded with corrosion inhibitors would be liberated to achieve self-healing effects.

2.4. Self-Healing Behavior

After immersing the samples with scratches in Hank's solution, images were taken after 15 min and 30 min. Surprisingly, the Silk-HNT/PA and Silk-HNT/Ce³⁺ coating system fully realized self-healing in only 15 min under the solution environment, as shown in **Figure 5**A. The healed scratches had an appearance similar to that of wound crusts. In addition, the
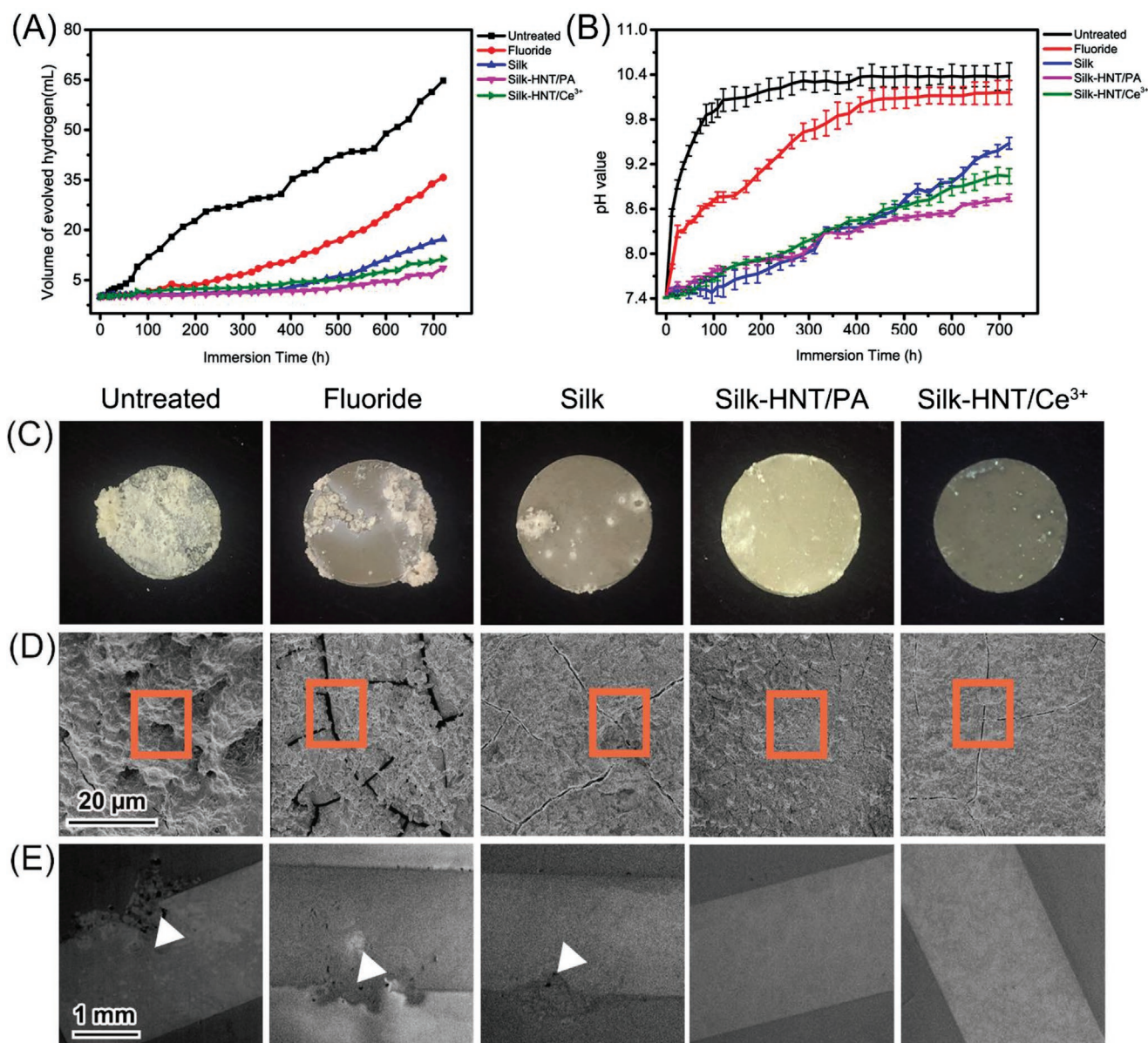
Figure 3. Surface morphology of samples after immersion for 30 days. A) Volume of evolved hydrogen, B) pH value, C) macrography characteristic, D) SEM images of sample surface, E) SEM images of sample cross-section.
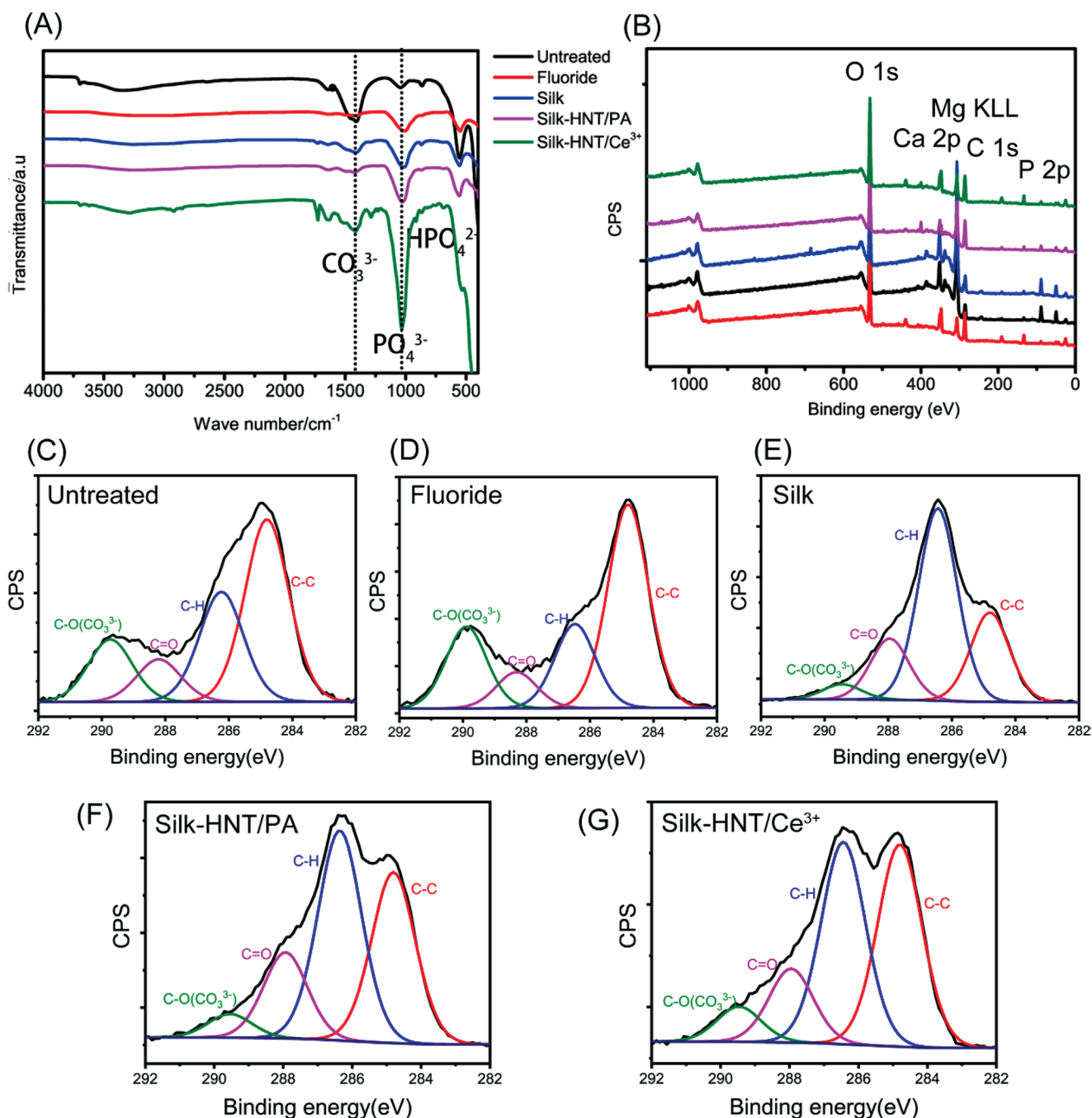
elements in the scratches after immersion were examined by EDS. The results show (Table S4, Supporting Information) that only O and Mg elements were detected at Silk scratches, while Silk-HNT/PA was rich in P and C (mainly due to PA), and Silk-HNT/Ce^{3+} was detected for element Ce. These characteristic elements at the scratches hint at the deposition of corrosion inhibitors, and thus the self-healing performance of the designed coatings.

2.5. pH Stimuli-Responsive Behavior of Corrosion Inhibitor

The pH stimuli-responsive behavior of the coatings was evaluated by immersing Silk-HNT/X samples in aqueous environments with pH 7.4 and 10.0. Because the corrosion inhibitor content was below the detection limit in the pH 7.4 solution, the amount of SiO$_2$ in the immersion solution was characterized to represent HNT content instead. As is shown in Figure 5B and 5C, Silk-HNT/X was stable in neutral environment and hardly released corrosion inhibitors, which accords with the stable secondary structure of silk in the coating. In the pH 10.0 solution, Silk-HNT/X continuously released the corrosion inhibitor, indicating pH stimuli-responsive characteristics. This was ascribed to the reversibility of residual random coils and α-helical structure in the silk, which would be negatively charged with a rise in local pH. Then the interactions were disconnected, leading to a elongated molecular conformation.[33] As a result, more HNT were released in the defects.

**ADVANCED
SCIENCE NEWS**

www.advancedsciencenews.com

NANO · MICRO

small

www.small-journal.com

Figure 4. Surface characteristics of each group after immersion in Hank's for 30 days. A) ATR-FTIR spectra, B) XPS analysis, C–G) the co-responding core-level spectra for C 1s of each group.

2.6. Electrochemical Impedance Testing

Because of the similar self-healing behaviors of the Silk-HNT/PA and Silk-HNT/Ce^{3+} systems in the scratch test, we chose Silk-HNT/PA for electrochemical impedance testing to further evaluate the coatings' self-healing behavior, with Silk as the control group. Electrochemical impedance spectroscopy (EIS) tests were performed after immersion in Hank's solution for 1 h, 3 h, 6 h, and 12 h, and analyzed by Novo 2.1

software and presented by the Nyquist plots, and Bode amplitude curve. To further interpret the EIS results, the equivalent electrical circuit (EEC) models were proposed for fitting the data. Constant phase element (CPE) instead of capacitance is used in the fitting procedure, while Rs is the solution resistance. All results are shown in **Figure 6** (Silk group is A1, A2, A3, Silk-HNT/PA group is B1, B2, B3). The EECs involved in Silk and Silk-HNT/PA are listed in Figure 6① and ②. The equivalent circuit models are Rs (QdlRct) (QbRb)
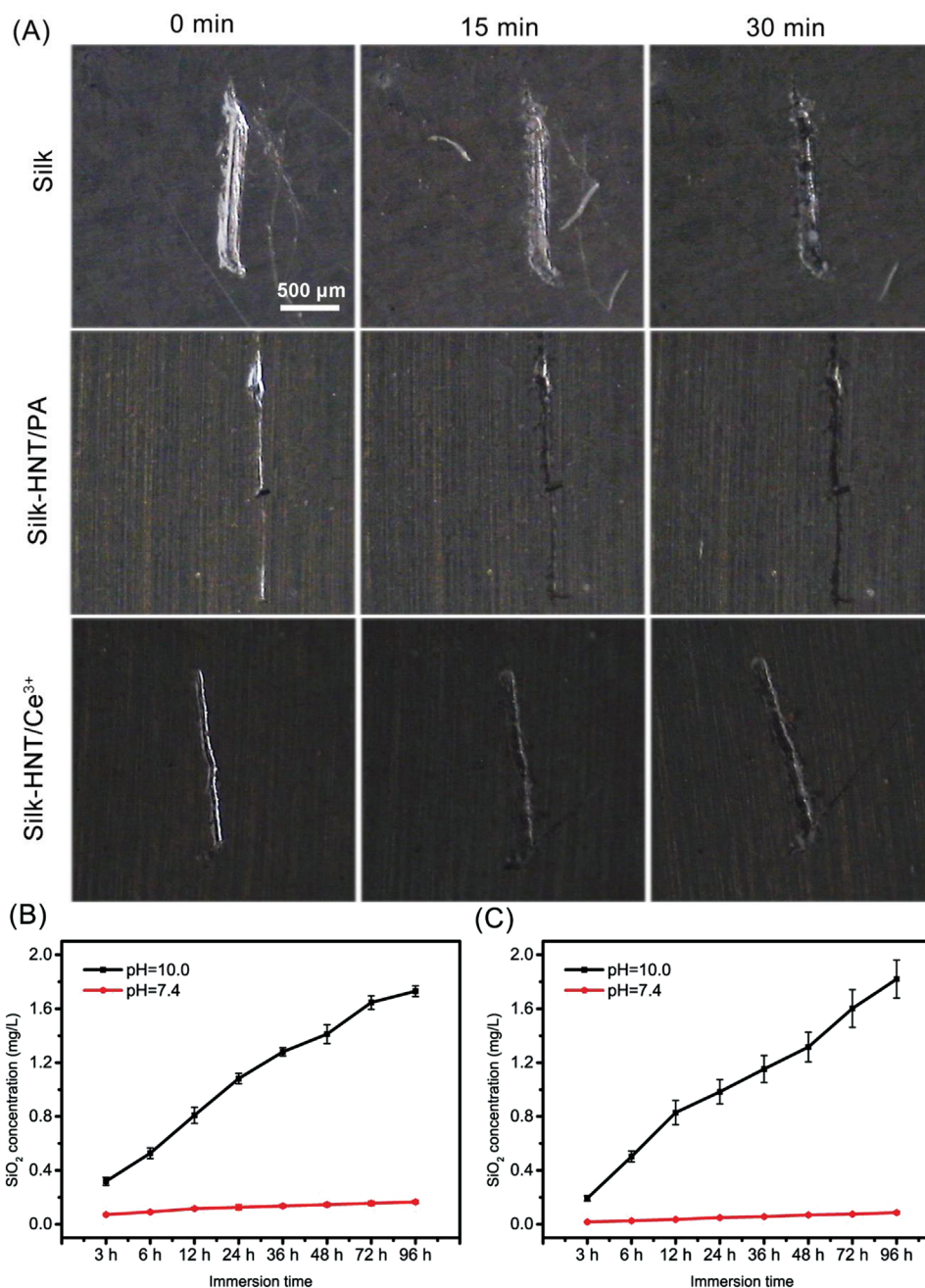
Figure 5. A) Optical imaging of scratch tests of the silk, Silk-HNT/PA, and Silk-HNT/Ce^{3+} group, B,C) pH stimuli-responsive behavior of each group in pH 7.4 and 10.0.

and Rs (QdlRct) (QbRb (RLL)). According to the definition of polarization resistance (Rp), its value dictates the difference between the actual impedance of the Nyquist diagram (when the frequency is equal to zero) and the resistance of the solution (Rs), and it is proportional to the corrosion resistance. Based on this, the Rp involved can be calculated using the following equations:

Figure 6①:

$$\frac{1}{R_P} = \frac{1}{R_{ct} + R_b} \tag{2}$$

Figure 6②:

$$\frac{1}{R_P} = \frac{1}{R_{ct} + \left(R_b^{-1} + R_L^{-1}\right)^{-1}} \tag{3}$$

The parameters obtained by the fitting and the polarization impedance (calculated according to the above formula) are summarized in Table S5, Supporting Information. The results show that the polarization resistance of Silk-HNT/PA decreased over time during the 3 h before immersion, indicating a wane

**ADVANCED
SCIENCE NEWS**
www.advancedsciencenews.com

NANO · MICRO
small
www.small-journal.com
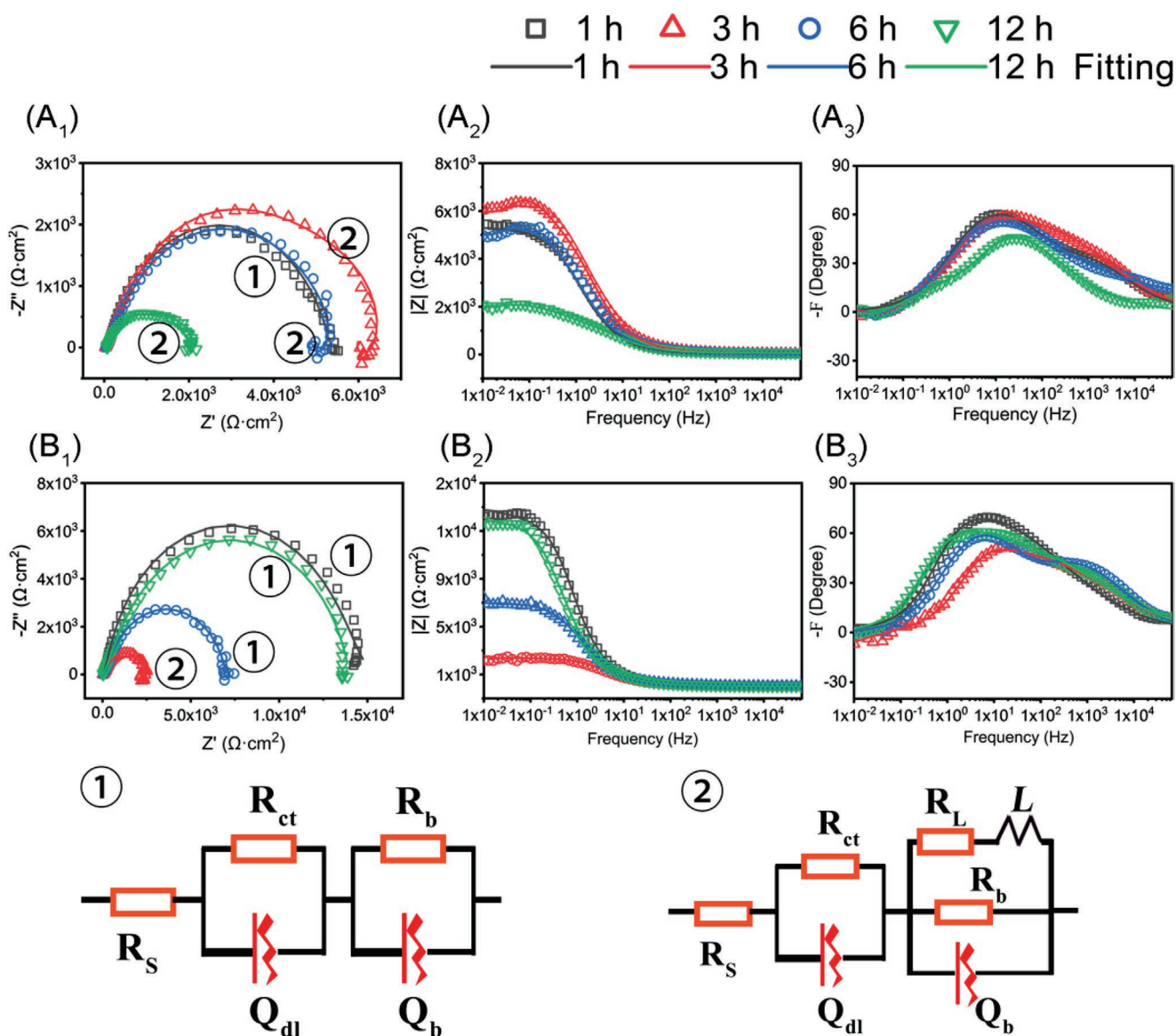
**Figure 6.** Electrochemical impedance spectroscopy (EIS) of A) the silk, B) Silk-HNT/PA, the equivalent electrical circuit (EEC) models of ①the silk, ②Silk-HNT/PA.

in corrosion resistance. During the immersion period of 3 to 12 hours, the polarization impedance gradually increased to eventually exceed the initial impedance value. This suggests that the surface corrosion resistance was restored, and thus self-healing in performance was achieved. For Silk, the impedance only gradually decreased with the immersion time, indicating a lack of self-healing behavior.

2.7. The Enhanced In Vitro Biocompatibility and Osteogenic Activity of Silk-HNT/PA Coating

We evaluated the cytoskeleton development and cell adhesion morphology of hBMMSCs cells within 24 h, both cultured on the sample surface and in sample extracts. As shown in **Figure 7**A, cells cultured on the Silk and Silk-HNT/X coatings

were fully extended with clear actin filaments. However, there were no normal cell on the untreated Mg-1Ca alloy sample surface, and little abnormal shape cell on the fluoride group. Cells cultured in sample extracts also indicate that the Silk and Silk-HNT/X coatings extracts spread well (Figure 7B). The number of adhered cells in the untreated Mg-1Ca alloy and the Fluoride group is less than the Silk and Silk-HNT/PA groups. These results indicated that the coatings enhanced the biocompatibility of untreated Mg-1Ca alloy. To investigate the effects of sample on cell proliferation, hBMMSCs were cultured in different extracts for 1 d, 3 d, 5 d. The cell activity was evaluated by a CCK-8 kit. As given in Figure 7C, both Silk and Silk-HNT/X groups better supported the proliferation of hBMMSCs. Using the negative group as a control, the cell viability can be 110% or more (shown in Figure 7C). Therefore, the silk-based coatings showed better biocompatibility to hBMMSCs.
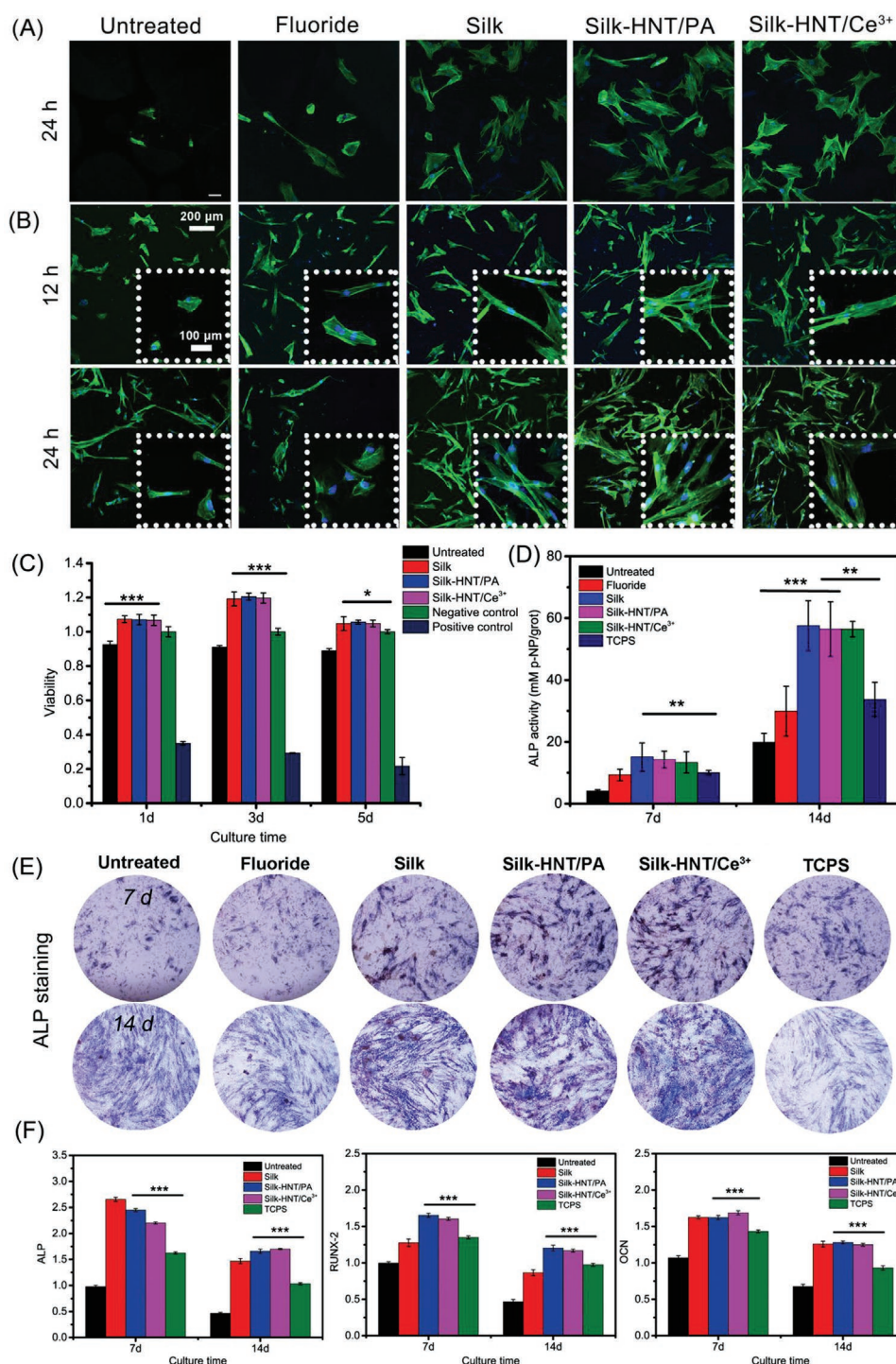
Figure 7. Adhesion and osteogenic differentiation properties of hBMMSCs. A) Adhesion of hBMMSCs cultured on sample surface for 24 h, B) adhesion of hBMMSCs cultured in sample extracts for 12 h and 24 h, C) cell viability of hBMMSCs cultured in each group for 1 day, 3 days and 5 days, D) alkaline phosphatase (ALP) activity quantification at day 7 and 14, E) ALP staining at days 7 and 14, F) the expression of osteogenic genes (*RUNX-2, OCN*, and *OSX)* of hBMMSCs at days 7 and 14. #P < 0.05.

The effects of samples on osteogenic differentiation of hBMMSCs were evaluated by characterizing the early, middle, and late osteogenic differentiation indicators. Both ALP activity quantitative measurement (Figure 7D) and qualitative ALP staining (Figure 7E) results show that Silk group and Silk-HNT/X

both had improved osteogenic differentiation compared to untreated Mg-1Ca alloy, fluorinated treatment, and tissue culture plates (TCPS). There was no significant difference amongst the silk fibroin-based coating groups. Specifically, the silk fibroin-based coating groups had higher ALP activity.

qPCR was used to detect the expression of osteogenesis-related genes *ALP, RUNX-2,* and *OCN* of hBMMSCs after cultivation for 7 days and 14 days. *ALP* is a specific expression gene in the early and middle stages of osteogenic differentiation, *OCN* is a specific expression gene in the middle and late stages of osteogenic differentiation, and *RUNX-2* mainly guides osteogenesis differentiation and is responsible for the integration and regulation of osteogenesis-related gene expression channels. Results (Figure 7F) show that the Silk and Silk-HNT/X groups were able to enhance the expression of *ALP, OCN* and *RUNX-2* genes. Impressively, the silk fibroin-based groups elicited a higher level of gene expression even when compared with cells grown in normal osteogenic induction culture medium. The results here confirm the appealing osteogenic potential of Silk and Silk-HNT/X, at the gene level, which agrees well with data in the previous section. Overall, both Silk and Silk-HNT/X can promote osteogenic differentiation and hence have potential in bone regeneration.

The Silk-HNT/PA coating significantly improved the in vitro biocompatibility and osteogenic activity of untreated Mg-1Ca alloys. This can be explained by the following aspects. Firstly, Silk-HNT/PA improves the corrosion resistance of the substrates, which is effective to control the release of Mg^{2+} and hydrogen, and decrease the local pH, so as to maintain an environment suitable for cell survival and thriving. Secondly, silk fibroin is known as a promising biomaterial with excellent osteogenic ability.[34] The osteogenesis potency of silk fibroin mainly arises from two aspects. One is that silk fibroin holds a unique β-sheet structure, similar to the type I collagen structure in natural bone. This structural resemblance enables silk fibroin to induce mineralization. In addition, silk fibroin can inhibit the expression of Notch pathway, and as a result, facilitate the expression of ALP and osteo-differentiation in osteoblasts. Thirdly, the corrosion inhibitor phytic acid ($C_6H_{18}O_{24}P_6$, PA) as an organic molecule extracted from plants has good biocompatibility.[35]

2.8. The Enhanced In Vivo Corrosion Resistance of Silk-HNT/PA coating

The in vivo degradation behavior and biocompatibility of Silk-HN/PA coating were investigated in the femora of SD rats. Untreated Mg-1Ca alloy was used as control. Micro-CT reconstruction of the samples (**Figure 8**A) illustrated that local corrosion of the untreated Mg-1Ca alloy was severe with massive corrosion pits prevailing. Whilst for the Silk-HN/PA group, the degradation was mild and uniform. After 12 weeks of implantation, the percentage of degradation for Silk-HN/PA group was 12.5%, while it was 33.3% for the untreated Mg-1Ca alloy. Therefore, Silk-HNT/PA coating greatly improved the corrosion resistance of Mg-1Ca alloy.

Hard tissue slices stained with methylene-blue/acid fuchsin were used to show the implant-tissue interface (Figure 8B). At 4 weeks, the untreated Mg-1Ca alloy underwent serious local corrosion. Bubbles were visible around the implant, due to the fact that hydrogen produced by rapid Mg degradation was difficult to diffuse away and thus accumulated in the surrounding tissue. By contrast, the Silk-HN/PA maintained its structural integrity. Meanwhile, a limited volume of new bone was formed around the Mg-1Ca alloy groups. At 12 weeks, large corrosion pits were observed in the untreated Mg-1Ca alloy. On the contrary, relatively compact tissue structure and only small corrosion pits were noticed in the Silk-HN/PA group, indicating better anticorrosion behavior. These results were consistent with those of the in vitro immersion test results.

To investigate the surface morphological change, as well as chemical compositions of the bone-implant interface, the implant-bone tissue sections were obtained and observed via SEM. As shown in Figure S2, Supporting Information, Silk-HNT/PA group assumed a uniform corrosion mode without localized corrosion, while Mg-1Ca alloy group underwent severe corrosion. After 4 weeks of implantation, the untreated Mg-1Ca alloy exhibited clear inhomogeneous corrosion, with the edges showing more corrosion pits, and larger bubble cavities appearing in the surrounding tissues. Silk-HNT/PA basically maintained the integrity of the sample, and no obvious bubble cavity was observed. After 12 weeks, the untreated Mg-1Ca alloy had severe local corrosion. The depths of the pits were close to the radius of the sample. On the contrary, the corrosion resistance of the coated samples had been greatly increased, despite slight random corrosion. The EDS mapping illustrated that the bone-implant interface was mainly composed of O, Ca and P. Since bone is rich in Ca and P, it can be concluded that de novo bone was deposited at the bone-implant interface, supporting satisfactory osteointegration.
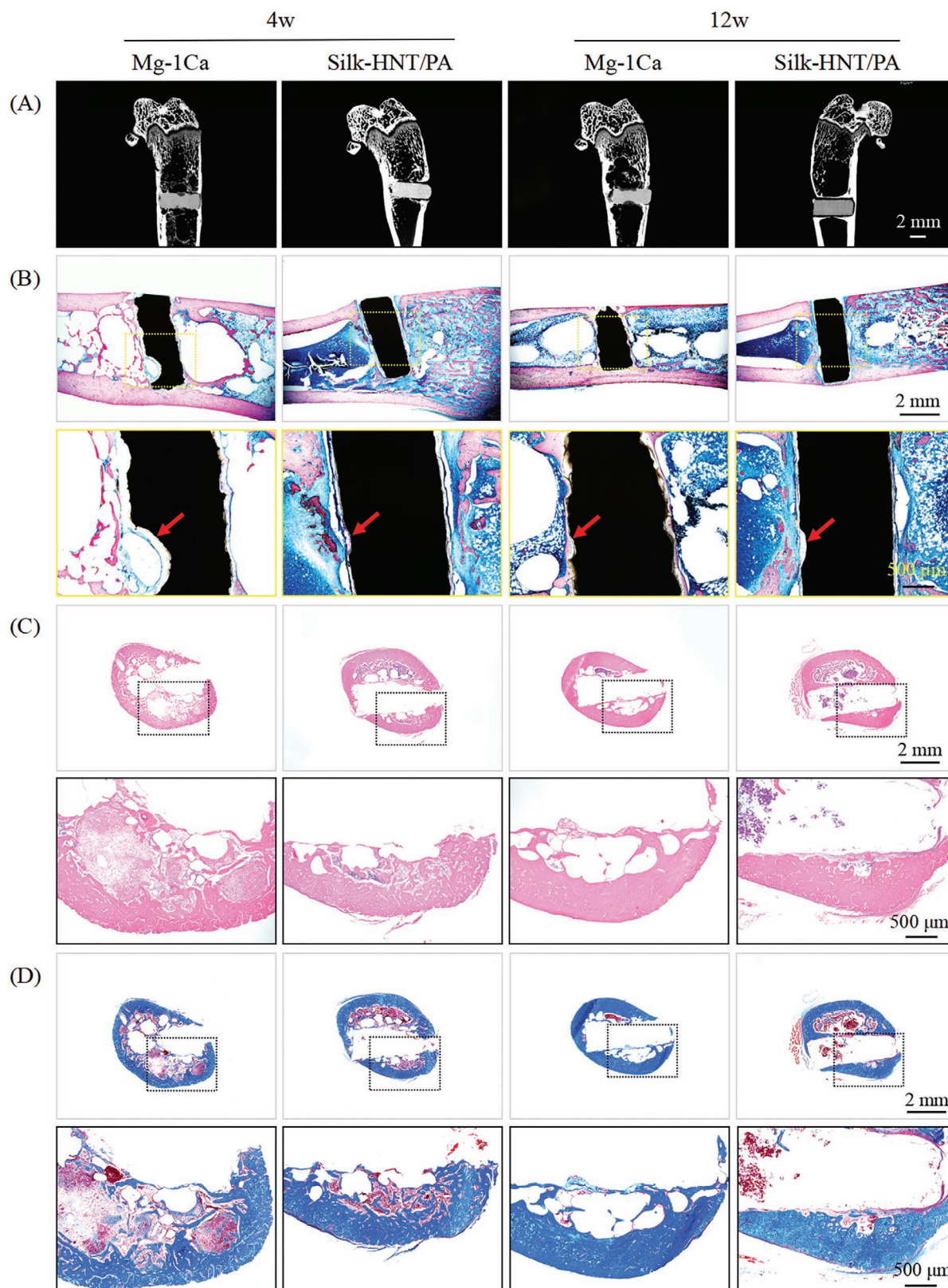
3. Conclusion

In summary, we here reported bio-compatible/-functional silk fibroin-based self-healing coatings (Silk-HNT/PA) for simultaneously enhancing the corrosion resistance and osteogenesis of Mg alloy osteoimplants. The major finding of this study is that HNT effectively enhanced the self-healing effects by vastly accelerating the healing. The resulting coating elicited fast self-healing response and remarkable anticorrosion ability, owing to the intriguing combination of silk fibrin (pH responsiveness), HNT (high loading capacity), and inhibitor PA (self-healing). Additionally, the coated implants had demonstrated great potential to boost osteogenic differentiation and osteointegration by in vitro and in vivo studies. The present work provided a simple but useful strategy for designing multifunctional coatings with bioadaptable corrosion resistance and desirable biofunctionality on Mg-based implants.

4. Experimental Section

Substrate Preparation: Extruded Mg-1Ca (wt.%) alloy rods were prepared as our previous work [36] and cut into cylinders (Φ12 mm × 2 mm for in vitro experiments; Φ2 mm × 6 mm for in vivo implantation). The samples were ground by SiC paper (400 grit, 800 grit, 1200 grit, and 2000 grit). Subsequently, all samples were ultrasonically washed by acetone, absolute ethanol and deionized water with for 10 min, respectively, followed by drying in open air.

Preparation of Self-Healing Coatings: The following chemicals were purchased: sodium hydroxide, HF (40% v/v), PA, and sodium phosphate from Beijing Chemical Works; cerium nitrate, HNTs, and

ADVANCED
SCIENCE NEWS
www.advancedsciencenews.com

NANO · MICRO
small
www.small-journal.com

Figure 8. In vivo performance of Mg-1Ca and Silk-HNT/PA rods after 4 and 12 weeks' implantation. A) Representative Micro-CT images of rat femora, B) representative histological observation of the femora hard tissue section stained with methylene-blue/acid fuchsin staining. The yellow rectangles are zoomed for further magnification. C,D) Representative histological observation of the HE and Masson staining. The black rectangles are zoomed for further magnification.

hexafluoroisopropanol (HFIP) from Sigma. All chemicals were in analytical grade and used as received.

Firstly, Samples were first immersed in boiling NaOH solution (200 g L^{-1}) for 3 h, and then rinsed with deionized (DI) water and dried in cold air. The resulting specimens were immersed in HF (40% v/v) at 60 °C for 6 h. Samples were washed by DI water and dried at room temperature (RT). The fluoride-treated samples were abbreviated as "Fluoride" in subsequent contexts.

Secondly, the silk fibroin solution was extracted following a previous protocol.[37] The resulting solution was frozen at −20 °C overnight and then lyophilized in a freeze-dryer for 24 h. The lyophilized silk fibroin was dissolved in hexafluoroisopropanol solution to provide a final concentration of 2 w/v%.

Third, loading of PA and Ce^{3+}. Two equivalents of HNTs (1.0 g) were prepared and vacuumed for 1 h, respectively. Then, two corrosion inhibitors, namely 10 mL 75% phytic acid (PA) and 10 mL saturated cerium nitrate (Ce(NO$_3$)$_3$) solution, were added respectively to each portion of HNTs. After stirring for 2 h under ambient condition, the mixture was taken to be centrifuged at 6000 rpm for 20 min. The precipitation was collected, and washed by centrifugation/redispersion cycles, and the final materials were dried overnight. All the supernatants after centrifugation were collected, which, together with the initial solutions, were characterized for P or Ce element contents by inductively coupled plasma mass spectrometry (ICP-MS, Agilent 7700X, USA). The inhibitor loading efficiencies by HNTs were determined as the elemental changes before and after centrifugation. The collected HNTs were dried and analyzed by TEM and XPS to confirm the loading of corrosion inhibitors. The HNTs loaded with PA or Ce are labeled as HNT/PA and HNT/Ce^{3+}, respectively. The two models for loading were depicted in Scheme 1A.

Forth, preparation of silk-HNT/X (PA, Ce^{3+}) composite coating. HNT/PA and HNT/Ce^{3+} were dissolved in DI water with a final concentration of 10% w/v. Small equivalents of the above solution were pipetted and added dropwise to the prepared silk fibroin solution under stirring. Finally, a solution with 0.2% w/v inhibitors was resulted and ultrasonically treated for 30 min to allow dispersion.

Then, for spinning coating, a spin coater (KW-4A, Si-you-yen®, Beijing, China) was employed as per our previous study.[21] Briefly, 50 μL of the prepared silk-HNT/X (PA, Ce^{3+}) solution was added to Mg-1Ca surface. Each spinning cycle consisted of a low-speed phase (500 rpm) for 12 s and a high-speed phase (4000 rpm) for 10 s. The above process was repeated for 5 times. Thereafter, 50 μL of pure silk fibroin solution was spun similarly on the sample surface, giving a capping layer to further prevent inhibitor leakages. The prepared samples were marked as "Silk-HNT/PA" and "Silk-HNT/Ce^{3+}". The coatings prepared by pure silk fibroin solution with identical parameters were used as control (spin-coated for 6 times) and labeled as "Silk". The experimental process is depicted in Scheme 1B.

Characterization of Silk-HNT/X (PA, Ce^{3+}) Coatings: The HNT, HNT/PA, HNT/Ce^{3+} were investigated by transmission electron microscope (FE-TEM, JEM-2100 F, JEOL, Japan), and field emission scanning electron microscope (FE-SEM, S-4800, Hitachi) equipped with an energy-dispersive spectrometer (EDS, Bruker QUANTAX, Germany) attachment. The chemical composition and elemental states of samples were determined by X-ray photoelectron spectroscopy (XPS, AXIS Ultra, Kratos) with Al Kα irradiation (hυ = 1486.71 eV).

The surface morphologies of the samples were observed by SEM. The functional groups of the obtained coatings were identified by Attenuated Total Reflectance-Fourier Transform Infrared analysis (ATR-FTIR, Thermo Fisher), using spectra recorded from 4000 cm^{-1} to 400 cm^{-1}. The characteristic peaks of functional groups were analyzed by peak fitting. The chemical composition and elemental states of the coatings were determined by XPS.

Self-Healing Behavior: An artificial scratch was done on one selected side of each coated sample using a sharp needle. The scratching was depth enough to reach the Mg-1Ca alloy substrate. The scratched samples (n = 5) were immersed in Hank's solution (NaCl 8.00 g L^{-1}, KCl 0.40 g L^{-1}, CaCl$_2$ 0.14 g L^{-1}, NaHCO$_3$ 0.35 g L^{-1}, MgSO$_4$·7H$_2$O 0.20 g L^{-1},

Na$_2$HPO$_4$·12H$_2$O, 0.12 g L^{-1}, KH$_2$PO$_4$ 0.06 g L^{-1}, pH = 7.4) at 37 °C for 15 min and 30 min to evaluate self-healing behavior. Optical images for each sample before and after immersion were acquired.

pH Response Ability: The self-healing coatings were prepared on glass sheets by the same method as described above. The samples were immersed in DI water with pH values of 7.4 and 10.0 for 12 h. The pH values were achieved by adding NaOH (0.1 mol L^{-1}). The solutions were collected at 1 h, 2 h, 3 h, 4 h, 5 h, 6 h, 12 h, 24 h, 36 h, 48 h, 72 h and 96 h. At each time point, fresh DI was used to replace the sample-conditioned solution. The amount of corrosion inhibitors (PA, Ce^{3+}) released under various pH conditions were analyzed by ICP-MS, with regard to the concentrations of P elements, Ce elements, and SiO$_2$ in the collected solutions.

In Vitro Corrosion Behavior: For each group, five duplicate samples were immersed in Hank's solution at 37 °C according to ASTM-G31-72.[38] Hydrogen evolution tests were carried out using a set-up described in previous study.[39] The pH values of the immersion solution, as well as the volumes of hydrogen generated, were recorded at given time points. After 30 days' immersion, the samples were withdrawn, carefully washed with DI, and dried in the open air. The surface and cross-sectional morphologies of samples were observed under SEM. The compositions of surface corrosion products were analyzed by XPS and ATR-FTIR.

Cell Culture: For in vitro biocompatibility tests, sample extracts were prepared in a cell incubator (100% relative humidity, 5% CO$_2$, 37 °C) using α-MEM supplemented with 10% fetal bovine serum (FBS) for 24 h, with an extraction ratio of 1.25 cm^2 mL^{-1}. Human bone marrow mesenchymal stem cells (hBMMSCs, Sciencell, San Diego, CA, US) and mouse osteoblast-like cells (MC3T3-E1) were cultured in α-minimal essential medium (α-MEM, Gibco, Grand Island, NY, US) supplemented with 10%FBS, 100 U mL^{-1} penicillin G, and 100 mg mL^{-1} streptomycin. The cells were cultured in 96-well plates (2000 cells per well), 48-well plates (4000 cells per well) and 24-well plates (25 000 cells per well), 6-well plates (10^5 cells per well), respectively. After 24 h of culture for cell attachment, the medium was discarded and replaced with the extracts. For all cell experiments, α-MEM containing 10% FBS was added per well into TCPS as control. The culture medium was refreshed every two days. All cell related experiments were repeated for no less than three times.

Cell Adhesion and Spreading: For fluorescence staining, sterile samples and glass plates were put in 24-well plates, and seeded with cells, which were then incubated with cell culture medium or the alloy extracts for 12 h and 24 h, respectively. The samples were rinsed with PBS, fixed by 4% w/v paraformaldehyde for 10 min and treated with 0.1% v/v Triton X-100 for 10 min. Then, FITC-phalloidin (1.0% v/v) was used to stain the cellular actin for 30 min at RT, and after that, DAPI (1 mg/mL^{-1}) was used to stain the cell nuclei for 5 min. The samples were washed for 3 times by PBS and captured by laser scanning confocal microscope (LSCM, Nikon, ALR-SI).

Cell Viability: The cell viability was evaluated with alloy extracts using cell counting kit (CCK8, Dojindo Laboratories, Kumamoto, Japan). The cells were cultured in different extracts in 96-well plates, α-MEM with 10% FBS, and that containing 10% dimethyl sulfoxide were used as the negative and positive control, respectively. After culturing for 1, 3 and 5 days, fresh cell culture medium supplied with 10% CCK-8 solution was added to replace the medium, and the cultures were incubated for another 2 h to allow formazan generation. The absorbance of each well was determined at 450 nm using a microplate reader. The cell viability was calculated by the following formula:

$$\text{Cell viability}\,(\%) = \left(\frac{[A]\text{sample} - [A]\text{positive}}{[A]\text{negative} - [A]\text{positive}} \right) \times 100\% \tag{4}$$

Alkaline Phosphatase (ALP) Staining and Quantification: To evaluate the effect of samples' extracts on the early osteogenic differentiation marker ALP, the cells were cultured in 12-well plates with sample extracts for 7 and 14 days. The cells were fixed in 4% paraformaldehyde and stained with BCIP/NBT ALP Color Development Kit (Beyotime, China) for qualitative imaging. Images for each well were acquired using an optical microscope (BX51, Olympus, Tokyo, Japan). For quantification

ADVANCED
SCIENCE NEWS

www.advancedsciencenews.com

NANO · MICRO
small
www.small-journal.com

of ALP activity, cells were rinsed by ice-cold phosphate-buffered saline (PBS) and then lysed in 1% Triton X-100 for 10 min on ice. Cells were treated with ultrasound on ice and centrifugated at 12 000 g for 30 min at 4 °C. Protein concentration were measured using bicinchoninic acid assay (BCA) protein assay kit (Pierce Thermo Scientific, USA), which correlates absorbance at 562 nm to protein concentration by using a pre-plotted bovine albumin standard curve. The ALP activity was tested by the colorimetrical production of p-nitrophenol (p-NP) via p-nitrophenyl phosphate (p-NPP)/endogenous ALP enzymatic reaction (Jiancheng, Nanjing, China). Finally, ALP activity were calculated according to our previous study.[40]

Real-Time Quantitative Polymerase Chain Reaction (qPCR): The relative expression of osteogenic genes *ALP*, *RUNX-2* and *OCN* of the hBMMSCs was analyzed by qPCR. Briefly, hBMMSCs were cultured by extracts for 7 and 14 days. Then, total cellular RNA was extracted by TRIzol reagent (Invitrogen, USA), and the RNA concentrations were determined with a spectrophotometer (NanoDrop 8000, Thermo, USA). The RNA was then reverse-transcribed into cDNA using a reverse transcription kit (TakaRa, Japan). The qPCR analysis was performed using SYBR Green PCR Master Mix (Roche Applied Science, Germany) on a QuantStudio 3 Real-Time PCR detection system (Applied Biosystems, USA). Primers (Table S6, Supporting Information) were designed according to a cDNA sequence from the National Center for Biotechnology Information database. The relative mRNA expression level of *ALP*, *RRUX-2* and *OCN* were normalized by housekeeping gene glyceraldehyde 3-phosphate dehydrogenase (GAPDH). Cycle threshold values were used to count the fold change using the ΔΔCt method. [41]

In Vivo Animal Implantation: Twenty 10-week-old specific pathogen-free male Sprague-Dawley (SD) rats were randomly assigned with Mg-1Ca and Silk-HNT/PA groups (*n* = 5). The animal experiments were approved by the Ethics Committee, Peking University Health Science Center, Beijing, China. Procedures were in accordance with requirements established by the Experimental Animal Ethics Branch (LA 2019019). To relieve sufferings, rats were anesthesia by 50 mg kg^{-1} pentobarbital sodium through intraperitoneal injection and lidocaine by local injection in the surgical area. A hole (Φ2 mm× 6 mm) was drilled in the rat distal femora bilaterally using a dental implant machine (SI-923, W&H Dentalwerk Burmoos GmbH, Austria). Samples were implanted and the wound was sutured. The rats were fed in an environmentally-controlled room. Rats were euthanized by overdosed pentobarbital sodium 4 and 12 weeks after operation. The femora, hearts, lives, spleens, lungs and kidneys were collected and kept in 10% neutral buffered formalin for 24 h at RT.

Alloy Degradation and Bone Formation Analysis: Micro-computed tomography (Micro-CT) scans were obtained using a high-resolution micro-CT scanner (Siemens, Munich, Germany). The following scanning parameters were adopted: voltage 60 kVp, current 220 μA, exposure time 1500 ms, specimen rotation 360°, effective pixel size 8.82 μM. Then, the femora were dehydrated using ascending concentrations of ethanol (from 75% to 100% ethanol) and embedded in polymethylmethacrylate. The specimens were cut to 200 μm using an EXAKT 300CP saw microtome, and the sections were further ground to 30–40 μm. Two pieces of sections were made for each specimen. One section was coated with a thin layer of gold to improve conductivity and examined by SEM-EDS. The other section was stained with methylene-blue/acid fuchsin stains. The mature degree of newly bone was also assessed by hematoxylin and eosin (HE) and Masson's staining. Briefly, specimens were decalcified in 10% ethylene diamine tetraacetic acid (EDTA) for 8 weeks, and then dehydrated in ethanol and dewaxing in xylene. Followed by embedding in paraffin, specimens were cut into 5-μm-thick sections and subsequently stained with HE and Masson. Representative images of stained sections were captured using an optical microscope (BX51, Olympus, Tokyo, Japan).

Statistical Analysis: All statistical analyses were expressed as the mean ± standard deviation and analyzed using SPSS 19.0 software (SPSS Inc., Chicago, IL, USA). Statistically significant was defined as *P* value <0.05 and determined by a one-way analysis of variance (ANOVA) followed by Tukey's post hoc tests.

Supporting Information

Supporting Information is available from the Wiley Online Library or from the author.

Acknowledgements

Conflict of Interest

The authors declare no conflict of interest.

Data Availability Statement

The data that support the findings of this study are available from the corresponding author upon reasonable request.

Keywords

[1] N. Li, Y. F. Zheng, *J. Mater. Sci. Technol.* **2013**, *29*, 489.
[2] Y. Zheng, X. Gu, F. Witte, *Mater. Sci. Eng. R-Rep.* **2014**, *77*, 1.
[3] M. Echeverry-Rendon, J. P. Allain, S. M. Robledo, F. Echeverria, M. C. Harmsen, *Materials Sci. Eng. C, Mater. Biolog. Appl.* **2019**, *102*, 150.
[4] H. Hornberger, S. Virtanen, A. R. Boccaccini, *Acta Biomater.* **2012**, *8*, 2442.
[5] Z. S. Seyedraoufi, S. Mirdamadi, *Mater. Chem. Phys.* **2014**, *148*, 519.
[6] X. N. Gu, N. Li, W. R. Zhou, Y. F. Zheng, X. Zhao, Q. Z. Cai, L. Ruan, *Acta Biomater.* **2011**, *7*, 1880.
[7] X. N. Gu, W. Zheng, Y. Cheng, Y. F. Zheng, *Acta Biomater.* **2009**, *5*, 2790.
[8] Y. Liu, D. Bian, Y. Wu, N. Li, K. Qiu, Y. Zheng, Y. Han, *Colloids Surf. B, Biointerfaces* **2015**, *133*, 99.
[9] J. Sun, J. Wang, H. Jiang, M. Chen, Y. Bi, D. Liu, *Mater. Sci. Eng. C, Mater. Biolog. Appl.* **2013**, *33*, 3263.
[10] P. Wang, P. Xiong, J. Liu, S. Gao, T. Xi, Y. Cheng, *J. Mater. Chem. B* **2018**, *6*, 966.
[11] H. Sampatirao, S. Amruthaluru, P. Chennampalli, R. K. Lingamaneni, R. Nagumothu, *J. Magnes. Alloy.* **2021**, *9*, 910.
[12] Y. Li, S. Zhao, S. Li, Y. Ge, R. Wang, L. Zheng, J. Xu, M. Sun, Q. Jiang, Y. Zhang, H. Wei, *Small (Weinheim an der Bergstrasse, Germany)* **2019**, *15*, 1904486.
[13] D. D. Zhang, F. Peng, X. Y. Liu, *J. Alloys Compd.* **2021**, *853*, 22.
[14] F. Zhang, P. F. Ju, M. Q. Pan, D. W. Zhang, Y. Huang, G. L. Li, X. G. Li, *Corros. Sci.* **2018**, *144*, 74.
[15] L. M. Calado, M. G. Taryba, M. J. Carmezim, F. Montemor, *Corros. Sci.* **2018**, *142*, 12.
[16] J. L. Chen, L. Fang, F. Wu, J. Xie, J. Hu, B. Jiang, H. J. Luo, *Prog. Org. Coat.* **2019**, *136*, 11.

[17] X. Wang, L. X. Li, Z. H. Xie, G. Yu, *Electrochim. Acta* **2018**, *283*, 1845.

[18] Q. Dong, X. Zhou, Y. Feng, K. Qian, H. Liu, M. Lu, C. Chu, F. Xue, J. Bai, *Bioactive Mater.* **2021**, *6*, 158.

[19] B. Li, R. Huang, J. Ye, L. Liu, L. Qin, J. H. Zhou, Y. F. Zheng, S. L. Wu, Y. Han, *Chem. Eng. J.* **2021**, *403*, 126323.

[20] P. Xiong, J. Yan, P. Wang, Z. Jia, W. Zhou, W. Yuan, Y. Li, Y. Liu, Y. Cheng, D. Chen, Y. Zheng, *Acta Biomater.* **2019**, *98*, 160.

[21] P. Xiong, Z. Jia, W. Zhou, J. Yan, P. Wang, W. Yuan, Y. Li, Y. Cheng, Z. Guan, Y. Zheng, *Acta Biomater.* **2019**, *92*, 336.

[22] A. C. Santos, C. Ferreira, F. Veiga, A. J. Ribeiro, A. Panchal, Y. Lvov, A. Agarwal, *Adv. Colloid Interface Sci.* **2018**, *257*, 58.

[23] D. Fix, D. V. Andreeva, Y. M. Lvov, D. G. Shchukin, H. Moehwald, *Adv. Funct. Mater.* **2009**, *19*, 1720.

[24] G. Cavallaro, S. Milioto, F. Parisi, G. Lazzara, *ACS Appl. Mater. Interfaces* **2018**, *10*, 27355.

[25] E. Askari, M. Mehrali, I. H. Metselaar, N. A. Kadri, M. M. Rahman, *J. Mech. Behav. Biomed. Mater.* **2012**, *12*, 144.

[26] J. M. Aamodt, D. W. Grainger, *Biomaterials* **2016**, *86*, 68.

[27] E. D. Pellegrino, R. M. Biltz, *Nature* **1968**, *219*, 1261.

[28] X. Cui, Q. Li, Y. Li, F. Wang, G. Jin, M. Ding, *Appl. Surf. Sci.* **2008**, *255*, 2098.

[29] C. H. Ye, Y. F. Zheng, S. Q. Wang, T. F. Xi, Y. D. Li, *Appl. Surf. Sci.* **2012**, *258*, 3420.

[30] R. Zhang, S. Cai, G. Xu, H. Zhao, Y. Li, X. Wang, K. Huang, M. Ren, X. Wu, *Appl. Surf. Sci.* **2014**, *313*, 896.

[31] Y. Wang, Y. Zhu, C. Li, D. Song, T. Zhang, X. Zheng, Y. Yan, M. Zhang, J. Wang, D. G. Shchukin, *Appl. Surf. Sci.* **2016**, *369*, 384.

[32] D. G. Shchukin, H. Mohwald, *Small* **2007**, *3*, 926.

[33] A. S. Lammel, X. Hu, S.-H. Park, D. L. Kaplan, T. R. Scheibel, *Biomaterials* **2010**, *31*, 4583.

[34] S. Midha, S. Murab, S. Ghosh, *Biomaterials* **2016**, *97*, 133.

[35] L. A. Hernandez-Alvarado, L. S. Hernandez, M. A. Lomeli, J. M. Miranda, L. Narvaez, I. Diaz, M. L. Escudero, *J. Alloys Compd.* **2016**, *664*, 609.

[36] Z. Li, X. Gu, S. Lou, Y. Zheng, *Biomaterials* **2008**, *29*, 1329.

[37] D. N. Rockwood, R. C. Preda, T. Yücel, X. Wang, M. L. Lovett, D. L. Kaplan, *Nat. Protoc.* **2011**, *6*, 1612.

[38] ASTM G31-72(2004), Standard Practice for Laboratory Immersion Corrosion Testing of Metals, **1990**.

[39] R. C. Zeng, L. Y. Cui, K. Jiang, R. Liu, B. D. Zhao, Y. F. Zheng, *ACS Appl. Mater. Interfaces* **2016**, *8*, 10014.

[40] W. Ge, Y. Liu, T. Chen, X. Zhang, L. Lv, C. Jin, Y. Jiang, L. Shi, Y. Zhou, *Biomaterials* **2014**, *35*, 6015.

[41] W. Ge, L. Shi, Y. Zhou, Y. Liu, G. E. Ma, Y. Jiang, Y. Xu, X. Zhang, H. Feng, *Stem Cells* **2011**, *29*, 1112.